Journal of Power Sources 198 (2012) 132–142

Contents lists available at SciVerse ScienceDirect

Journal of Power Sources

journal homepage: www.elsevier.com/locate/jpowsour

Anode and cathode overpotentials and temperature profiles in a PEMFC

O.E. Herrera [a,c], D.P. Wilkinson [b,c], W. Mérida [a,c,*]

[a] Department of Mechanical Engineering, University of British Columbia, Vancouver, BC V6T 1Z4, Canada
[b] Department of Chemical and Biological Engineering, University of British Columbia, Vancouver, BC V6T 1Z4, Canada
[c] Clean Energy Research Center (CERC), University of British Columbia, Vancouver, BC V6T 1Z4, Canada

ARTICLE INFO

Article history:
Received 18 June 2011
Received in revised form
16 September 2011
Accepted 17 September 2011
Available online 21 September 2011

Keywords:
Fuel cell
Overpotential
Segmented
Thermal effects

ABSTRACT

The separate anodic and cathodic overpotentials in a proton exchange membrane fuel cell (activation, ohmic, concentration and mass transport) were measured in conventional and segmented hardware via reference electrodes, and multi-component gas analysis. The results show that the anodic overpotentials cannot be ignored, even when the operating conditions are changed at the cathode only.

Under drying conditions the difference in the current density across the active area creates in-plane thermal gradients due to inhomogeneous reaction rates, and water phase changes. The resulting inhomogeneous temperature distributions can result in membrane and electrode degradation.

The combination of reference electrodes and multi-component gas analysis enables the measurement and calculation of kinetic and diffusion parameters that can be used for modeling, and improved fuel cell design, efficiency, and durability.

1. Introduction

The proton exchange membrane fuel cell (PEMFC) working voltage is determined by the intrinsic losses within the ionic conductor, and the membrane electrode assembly (MEA.) The deviations from the ideal equilibrium potential E_e are called overpotentials (η), and they reduce the useful cell voltage (E_{cell}). The overpotentials are commonly classified into four main categories: activation, diffusion, ohmic, and crossover:

$$E_{cell} = E_e - \eta_{A,a} + \eta_{A,c} - \eta_{D,a} + \eta_{D,c} - E_\Omega = E_e - \Sigma_\eta \quad (1)$$

In Eq. (1), the crossover overpotential does not appear explicitly, but its effect can be included by correcting the measured current density to account for fuel and oxidant leaks across the membrane. In conventional PEMFC technology, the hydrogen crossover is more common, and it translates into small current losses ranging from 0.12 to 7.8 mA cm^{-2}. The actual magnitudes depend on the membrane thickness, the temperature, the pressure, and the relative humidity (RH) during operation [1–3].

The effective current density (i) reported in this work is the sum of the measured current density (i^*) plus the crossover current density (i_x) as shown in Eq. (2):

$$i = i^* + i_x \quad (2)$$

The magnitude of i_x can be obtained by voltammetric measurements and may vary depending on the humidity, temperature and pressure. However, it is a small correction at practical current loads, and hereinafter we use the constant $i_x = 2.8$ mA cm^{-2}, which was obtained from a hydrogen/nitrogen cell operating at 2.04 atm and 298 K with a fully humidified membrane [4].

The ohmic losses, E_Ω, include electronic and ionic contributions from the anode, the cathode, and the membrane. The total electronic resistance includes contact and bulk components ($R_{contact}$, and $R_{electronic}$, respectively) resulting from the overall assembly (MEA, bipolar plates, etc.).

$$E_\Omega = iR = i(R_a + R_c + R_m) + i(R_{electronic} + R_{contact}) \quad (3)$$

The combined contact and bulk resistances ($R_{contact} + R_{electronic} = 5 \times 10^{-3}\ \Omega\,cm^2$) were measured using a graphite separator instead of the MEA. We assumed that these contributions remain constant for our experimental configuration and operating conditions. After correcting the ohmic potential for these resistances, the ionic resistances in the membrane (R_m), the anode (R_a), and the cathode (R_c) can be measured. The cathodic and anodic resistances can be isolated through the use of a reference electrode, and the membrane contribution can be further separated into two topological contributions (from the anode and cathode sides):

$$E_\Omega = i(R_a + \alpha R_m) + i(R_c + \beta R_m) + i(5 \times 10^{-3}\ \ \Omega\ \ cm^2) \quad (4)$$

In Eq. (4), α and β are two experimental anodic and cathodic factors ($\alpha + \beta = 1$), whose dependence on the experimental geometry

* Corresponding author at: Department of Mechanical Engineering, University of British Columbia, Vancouver, BC V6T 1Z4, Canada. Tel.: +1 604 822 4189; fax: +1 604 822 2403.
E-mail address: walter.merida@ubc.ca (W. Mérida).

0378-7753/$ – see front matter.
doi:10.1016/j.jpowsour.2011.09.042

Nomenclature

List of symbols

$A_{Pt,elec}$	mass-specific surface area of supported Pt available for the reaction ($m^2_{Pt}\,g^{-1}_{Pt}$)
b_a	anodic Tafel slope (V decade$^{-1)}$
b_c	cathodic Tafel slope (V decade^{-1})
D	diffusion coefficient ($m^2\,s^{-1}$)
E_{air}	cell potential when using air (V)
E_e	equilibrium potential (V)
E_{O_2}	potential when using pure oxygen (V)
E_Ω	ohmic potential losses (V)
F	Faraday's constant (96485 C mol^{-1})
i	current density (A cm^{-2})
i_0	exchange current density (A cm^{-2})
i_L	limiting current density (A cm^{-2})
i_x	crossover current density (2.8 mA cm^{-2})
K	thermal conductivity (mW m^{-1} K^{-1})
L	electrode areal loading of supported Pt catalyst ($mg_{Pt}\,cm^{-2}$)
m	equivalence constant (0.85–1)
n	number of electrons involved in a reaction
p_{air}	partial pressure of air (atm)
p_{H_2}	partial pressure of hydrogen (atm)
p_{O_2}	partial pressure of oxygen (atm)
Q_a	anodic heat (W)
Q_c	cathodic heat (W)
Q_{Total}	total heat (W)
R	resistance ($\Omega\,cm^2$)
R_a	anode resistance ($\Omega\,cm^2$)
R_c	cathode resistance ($\Omega\,cm^2$)
$R_{contact}$	contact resistance ($\Omega\,cm^2$)
$R_{electronic}$	electronic resistance ($\Omega\,cm^2$)
R_g	universal gas constant (8.3145 J mol^{-1} K^{-1})
RH	relative humidity (%)
R_m	membrane resistance ($\Omega\,cm^2$)
T	temperature (K)
α	anode resistance coefficient
α_a	anodic charge transfer coefficient
α_c	cathodic charge transfer coefficient
β	cathode resistance coefficient
$\Delta E_{O_2/air}$	potential difference between the potential when using pure oxygen and air (V)
$\Delta G_{343,a}$	Gibbs free energy change at 343 K at the anode (J mol^{-1})
$\Delta G_{343,c}$	Gibbs free energy at 343 K at the cathode (J mol^{-1})
$\Delta H_{343,a}$	enthalpy change at 343 K at the anode (J mol^{-1})
$\Delta H_{343,c}$	enthalpy change at 343 K at the cathode (J mol^{-1})
ΔH_{vap}	enthalpy of vaporization at 343 K at the cathode (J mol^{-1})
ΔP_c	gas pressure drop at the cathode (atm)
ΔP_c	gas pressure drop at the anode (atm)
η	overpotential (V)
$\eta_{A,a}$	anodic activation overpotential (V)
$\eta_{A,c}$	cathodic activation overpotential (V)
$\eta_{D,a}$	anodic diffusion overpotential (V)
$\eta_{D,c}$	cathodic diffusion overpotential (V)
η_{MT}	mass transport overpotential (V)
σ	standard deviation (V)

is explained in Section 2. The resistances in Eq. (4) include the ionomer ionic resistance for the anode and cathode, separately.

The activation loss or activation overpotential is mainly due to the cathodic oxygen reduction reaction (ORR). Its relationship to the current density (i) can be described using the Butler–Erdey–Grúz-Volmer equation:

$$i = i_0 \left(\exp\left(\frac{\alpha_a F}{R_g T}\right) \times \eta_{Act,a} - \exp\left(\frac{\alpha_c F}{R_g T}\right) \times \eta_{Act,c} \right) \quad (5)$$

In Eq. (5) the exchange current density (i_0) is the magnitude of the current density of both the anode and cathode at equilibrium. The factors α_a and α_c represent the anodic and cathodic transfer coefficients, respectively. They can be interpreted as the fractional change in the overpotential that leads to a change in the electron transfer rate.

Assuming that one of the reactions is dominant, the anodic and cathodic activation losses can be expressed by a Tafel approximation:

$$\eta_{A,a/c} = b_{a/c} \times \ln\left(\frac{i}{i_{0,a/c}}\right) \quad (6)$$

where $\eta_{a/c}$ is the dominant anodic or cathodic overpotential, $b_{a/c}$ is the anodic or cathodic Tafel slope, and $i_{0,a/c}$ is the exchange current density for the anode or the cathode, respectively. To account for differences in experimental setups, the cell potential must also incorporate the characteristics of the catalyst layers [2,5]. With these considerations, equation 6 becomes:

$$\eta_{A,a/c} = b_{a/c} \times \ln\left(\frac{i}{10 \times L_{a/c} \times A_{Pt,elec} \times i_{0,a/c(p)}}\right) \quad (7)$$

where L is the electrode areal loading of supported Pt catalyst in $mg_{Pt}\,cm^{-2}$ geometric, $A_{Pt,elec}$ is the mass-specific surface area of supported Pt available for the reaction in $m^2_{Pt}\,g^{-1}_{Pt}$ (average of $75\,m^2_{Pt}\,g^{-1}_{Pt}$, from the literature [2]), and i_0 is a function of the reactant partial pressures at the anode and the cathode ($i_{0,a}(p_{H_2})$ and $i_{0,c}(p_{O_2})$, respectively). At low current densities ($i < 200\,mA\,cm^{-2}$) the typical values of the Tafel slope for the cathode range between 59 and 64 mV decade^{-1}. At higher current densities, the slope may be greater, non-constant or inaccessible. The exchange current density ($i_{0,c}$) ranges between 0.8×10^{-9} and 8.7×10^{-9} A cm^{-2} [2].

In most of the reported work, the anodic activation overpotential was either neglected or considered insignificant. In this work, the anodic overpotentials are not neglected because our results indicate that they can be significant even at open circuit conditions (see Section 3).

The diffusion overpotential includes transport or concentration losses, and it can be described after obtaining the effective current density (i) and the limiting current density (i_L) as shown in Eq. (8).

$$\eta_d = \frac{R_g T}{F} \times \ln\left(1 - \frac{i}{i_L}\right) \quad (8)$$

The expression in Eq. (8) is derived for a reaction under mass transport control, provided that the electron transfer rate constant is always large and that the surface concentration is negligibly small or zero [6].

The distinct losses (and their associated physical phenomena) make it evident that voltage measurements across whole cells do not provide electrode-specific information. Hence, especial techniques are required to discern the effects occurring at the anode and the cathode (e.g., reference electrodes and multi-component gas analysis).

In prior work, we have reported overpotential measurements via reference electrodes at constant conditions [7]. Six reference electrodes were located in isolated chambers with a constant supply of humidified H_2 at a constant temperature and pressure. The chambers were located around the perimeter of the fuel cell's active area. In this work, the reference electrode potentials were corrected with proton concentrations of $[H^+] = 0.54$ M, and $[H^+] = 0.95$ M for fully saturated and dehydrated Nafion® membranes, respectively.

Recent work by Spry and Feyer determined these values using pyrene derivative photoacids and compared the pH values to HCl kinetics [8].

The reference electrode measurements were coupled with multi-component gas analysis and high frequency resistance (R_{HF}) measurements. The R_{HF} corresponds to the extrapolated real-axis intercept for electrochemical impedance spectroscopy spectra plotted on the Argand plane [9]. The reported frequency ranges vary, but they usually include measurements at frequencies larger than 1 kHz.

The principle behind multi-component gas analysis is the use of pure oxygen, heliox (helium 79%/oxygen 21%), and nitrogen/oxygen (79/21%), as the oxidant streams [2,10–13]. The varying composition and oxygen concentration result in changes in the oxygen and water diffusivity in the gases and through the membrane. With these three combinations it is possible to obtain quantitative values of the activation, mass transport and concentration losses [10,11,13]. The potential response while using pure oxygen can be used to calculate the activation overpotentials because the corresponding diffusion overpotentials are small or negligible. The difference between the cell potential running on heliox and the potential while using oxygen can be used to calculate the concentration losses. The mass transport overpotentials in heliox are negligible up to 1 A cm^{-2} [2,14,15] due to the higher diffusivity of O_2 in helium ($D_{O_2/He} = 0.42$ cm^2 s^{-1} at 270 kPa$_{abs}$ and 80 °C) compared to the corresponding value in nitrogen ($D_{O_2/N_2} = 0.11$ cm^2 s^{-1} at 270 kPa$_{abs}$ and 80 °C)[2]. Thus, the difference between the potential response while using air and the potential response while using heliox can be used for obtaining the mass transport losses. The combined concentration and mass transport losses represent the overall diffusion overpotential.

All the overpotentials vary across the active area as the temperature, the relevant reactant pressures, and the relative humidity change throughout the flow-field. Previous efforts have investigated these variations via segmented cell hardware, and localized current, temperature, and pressure measurements [10,16–21]. In the present work, we extend these techniques by correlating localized overpotential measurements to the associated current distributions via thermal analysis. We begin by noting that the net heat generation rates depend on the (exothermic) enthalpy of reaction at the cathode, the (endothermic) enthalpy of reaction at the anode, and the phase changes of water in the MEA layers [10,22].

The heat capacity of liquid water (74.5 J mol^{-1} K^{-1} at 298 K and 10^5 Pa) is approximately three times larger than that of the relevant gases (oxygen, nitrogen and hydrogen) at similar conditions. Moreover, the heat of vaporization or condensation (±43.98 kJ mol^{-1} at 298 K, and 10^5 Pa) corresponds to approximately 15%or 18% of the enthalpy of reaction (−285.8 kJ mol^{-1}or −241.82 kJ mol^{-1} at 298 K and 10^5 Pa, for water produced in liquid or vapour form respectively). Hence, the thermal gradients associated with water phase changes are significant, and they can stress, modify, or degrade the MEA layers and interfaces [22].

In the following sections, we present spatially resolved and isolated overpotential measurements at the anode and the cathode of a PEMFC under load. We then correlate these losses to the operating conditions and the heat production in the MEA.

2. Experimental

2.1. Hardware and MEA

The fuel cell hardware used in the present work has been described previously [7,23]. The flow-fields consisted of a single pass serpentine channel in a co-flow configuration (Fig. 1). The fuel cell was heated with water flowing at the back of the anode and cathode plates. All the experiments were carried out with

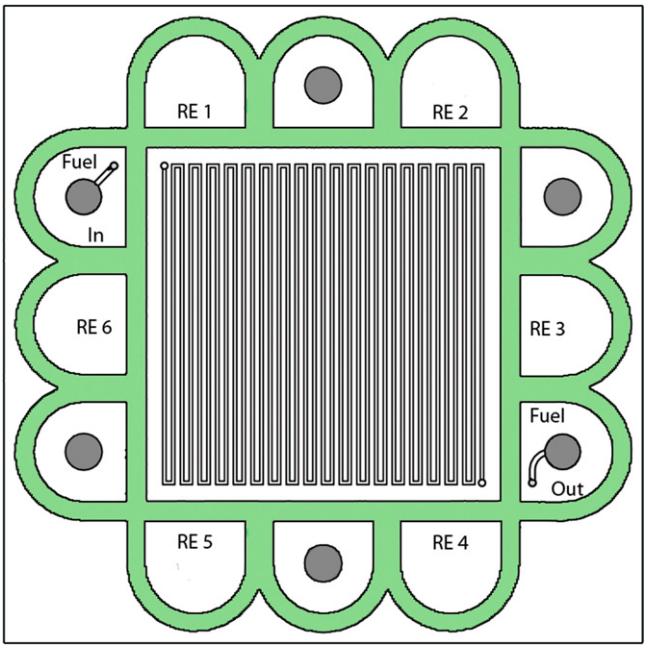

Fig. 1. Schematics of the anodic graphite plate with flow-field and the 6 reference electrodes locations in the isolated chambers.

Table 1
Membrane electrode assembly and flow-field details.

Catalyst loading anode 20% Pt/C (L_a, mg Pt)	0.3
Catalyst loading cathode 20% Pt/C (L_c, mg Pt)	0.7
Membrane	Nafion 115
Gas diffusion layer with microporous layer	SGL carbon 25 BC
Active area (cm^2)	49
Number of channels	27
Channel length (mm)	176.8
Cathode channel width (mm)	1.575
Cathode channel depth (mm)	1.270
Cathode landing width (mm)	0.864
Anode channel width (mm)	1.270
Anode channel depth (mm)	0.508
Anode landing width (mm)	1.168

Table 2
Operating conditions for normal, flooding and dry experiments. The stoichiometric flows, the inlet pressure, the temperature of the cell and the dry gases were maintained constant.

Test	Conditions	Value
Normal	DPT anode (°C)	75
	DPT cathode (°C)	75
Flooding	DPT anode (°C)	95
	DPT cathode (°C)	95
Dry	DPT anode (°C)	0
	DPT cathode (°C)	0
Fuel cell and gas temperatures are maintained constant (°C)		75
Bladder pressure (atm)		8.15
Inlet pressure (atm)		3.04
Stoichiometry of anode		1.5
Stoichiometry of cathode		2

custom-made, 49 cm^{2}MEA described in Table 1 (IonPower, New Castle, DE, USA). The MEA type was selected to facilitate the reproducible simulation of flooding and dehydration failures, not to obtain optimum performance. A 500 W Fuel Cell Test Station (Arbin Instruments, College Station, TX, USA) was used to control the flow rate, humidity, temperature and pressure of the gases supplied. In all cases, the cell temperature was approximately 75 °C (see Table 2 and Section 3). The gas inlet temperatures were maintained

constant and the dew point temperatures (DPT) were modified to change the level of hydration in the fuel cell. A separate subsystem was used to provide the constant conditions required for the reference electrodes in the isolated chambers (a constant flow of fully humidified hydrogen at 75 °C and 1 atm). The reference electrodes consisted of small patches of the catalyst used on the anode side in contact with 50 μm platinum wires coated with a 25 μm layer of Teflon®. A short (2 mm) section of the Teflon® layer was removed to expose the platinum. The platinum was then platinised and placed in the isolated chambers. An applied pressure of 7.82 atm was sufficient to maintain electrical contact between the reference electrodes and the platinum wires.

The high frequency resistances were measured by a Solartron 1250 Frequency Response Analyzer (London Scientific, London, Ontario, Canada) to validate the use of a GwINSTEK LCR-821 impedance meter (Instek, Concord, Ontario, Canada) operating at 1 kHz. The resistances were measured between the anode and the cathode, the anode and the reference electrode, and the cathode and the reference electrode. Previous work indicates that electrode misalignment [9,10,24] and water concentration gradients through the membrane can affect the impedance measurements [25]. In our measurements, both effects were minimised by separating the reference electrodes from the active area by a distance that was more than ten times the thickness of the membrane as recommended by Gerteisen [25]. Moreover, both sides of the membrane where the reference electrode was located were exposed to fully humidified gases. The resistance measured between the reference electrode and the cathode included the membrane resistance (B–P in Fig. 2).

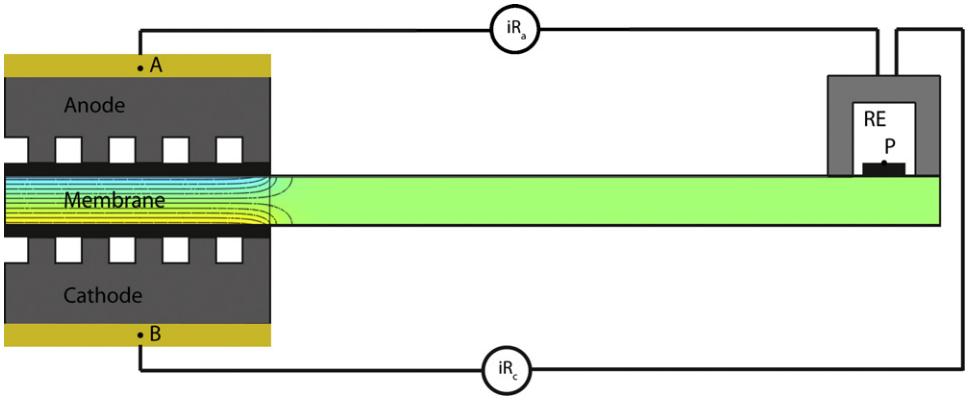

Fig. 2. Reference electrode HFR measurements from node A to B and node B to P. The drawing is not to scale, but the potential lines remain constant up to the reference electrode.

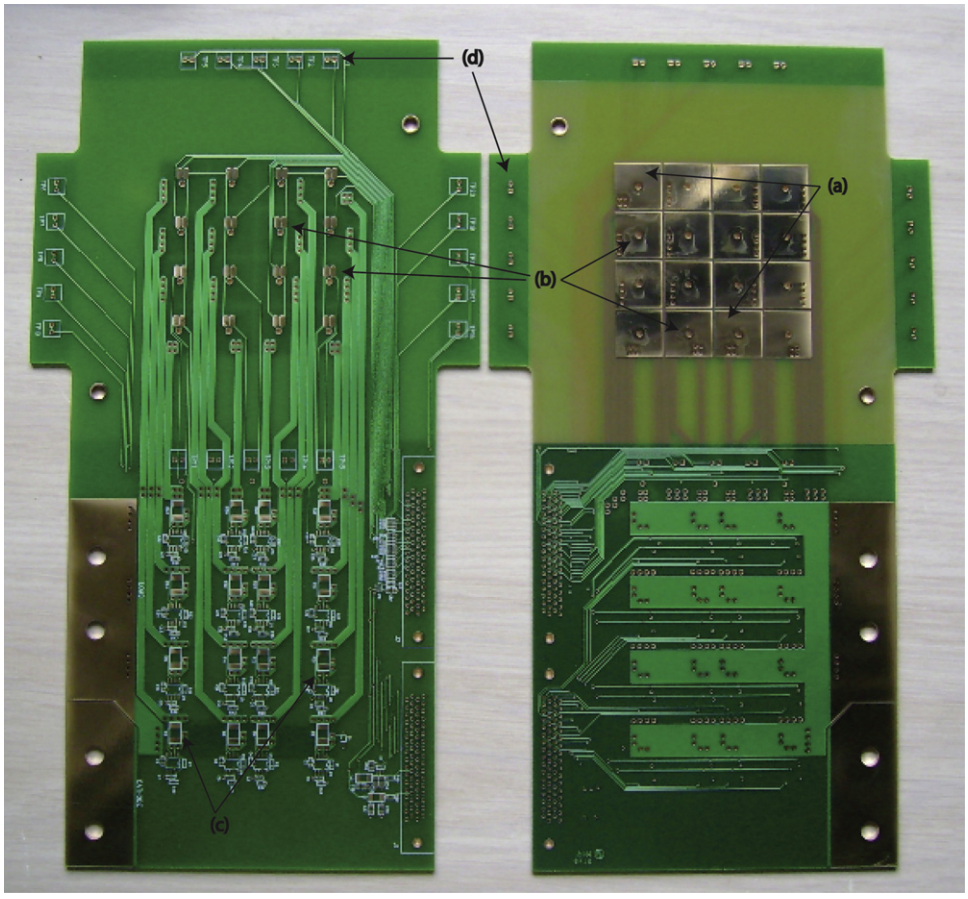

Fig. 3. Printed circuit board (PCB) with the current collectors (a), thermistors (b), resistors (c), and contact for the reference electrodes (d) for the segmented cathode plate.

With this arrangement, the potential lines, created by the anode and cathode, remain constant at point P (where there reference electrode measurement was carried out).

For the segmented cell results, the cathode flow field was divided into 16 segments and used in a co-flow configuration with the anode flow-field. The anode and cathode plates had the same flow-field profile to enhance sealing and maintain a homogeneous pressure distribution. The current from the segmented plate was collected by a printed circuit board (PCB) with gold plated contacts as shown in Fig. 3. The current was then converted to voltage via shunt resistors (c) and the associated voltage was amplified prior to being recorded by a data-acquisition system. Each of the current collectors (a) shown in Fig. 3 had a General Electric MC65F103B thermistor in the middle (b). The PCB also had 20 extra contacts for the connection of the reference electrodes, (d) and all the signals were collected by a PXI 6255 card with compatible LabViewsoftware (National Instruments, Austin, TX, USA).

2.2. Operating conditions

The fuel cell was operated under different loads (5–1200 mA cm^{-2}) for 15–30 min to obtain the average potential values for the polarization curves. Each polarization curve was run at least two times with increasing current and one time with decreasing current to quantify the possible hysteresis. Table 2 summarizes the operating conditions for the normal, flooding, and dehydrating experiments.

3. Results

3.1. Fuel cell overpotentials

Fuel cell performance losses for the anode and the cathode were isolated as shown in Fig. 4. These losses were further separated by adopting the following conventions for both electrodes.

The activation losses were obtained by subtracting the pressure- and temperature-corrected ideal equilibrium potential from the *iR* corrected performance with pure oxygen ($\eta_A = E_e - E_{O_2}$). The concentration losses were the difference between the *iR* corrected potential with oxygen and the *iR* corrected potential with heliox. The mass transport losses are the difference between the *iR* corrected potential with heliox and the *iR* corrected potential with air. The measured overpotentials and their calculated constants are summarized in Table 3. The differences between the calculated and the measured limiting current density (Table 3 and Fig. 4, respectively) can be related to voltage differences of 10–20 mV, which were within our experimental error range (e.g., the standard deviation, σ, between different MEA samples was approximately 15 mV). Even these small error scan cause large variations in the exponential expressions used in Table 3.

Under all the conditions, the largest contributions are from the cathodic activation overpotentials. These losses are attributed to the poor kinetics of ORR, and they are the limiting performance factor for state-of-the-art MEAs [26,27]. More detailed information on the ORR can be obtained by several methods [2,5,28]. In most cases, the analysis begins with two fundamental equations:

$$i \propto (p_{O_2})^m \quad \exp\left(\frac{-E}{b}\right) \tag{9}$$

$$E = E_{rev} + \eta \tag{10}$$

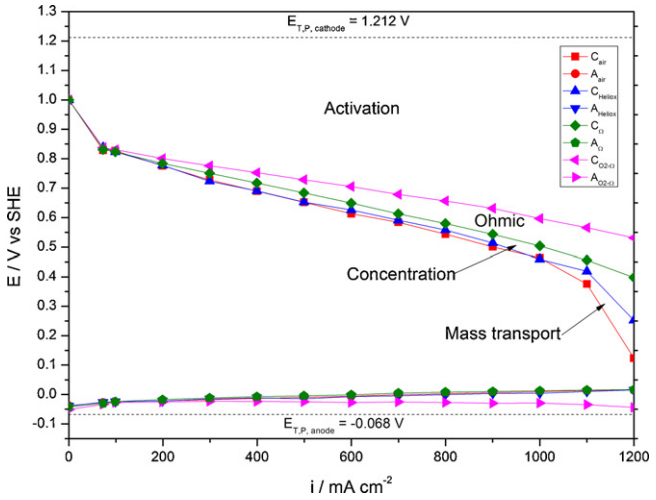

Fig. 4. Measured anodic and cathodic overpotentials obtained from using different gases with different diffusion coefficients in the cathode and the ohmic losses obtained from high frequency impedance measurements.

Table 3
Measured values for the potential losses obtained from Fig. 4 and their values at a current density of 1 A cm^{-2}. i_x = 2.8 mA cm^{-2} at 2.04 atm, 298 K, and a fully humidified membrane. The limiting current (i_L) was calculated at 3 different current densities (L: 5, M: 500, H: 1000 mA cm^{-2}). The values of i_L are different because a small measured overpotential value has a large effect on the calculation of i_L.

Expression	Parameters	Anode	Cathode	Units	Measurement method
$\eta_A = b \ \ln \ \frac{i}{i_o}$	{b}	{0.006}	{0.073}	{V}	Tafel diagram
	(i_o)	(7.70×10^{-5})	(1.13×10^{-9})	(A cm^{-2})	
$E_\Omega = iR$	$i\alpha R + i\beta R$	0.0411	0.0749	Ω cm^2	HFR measurement
$\eta_d = \frac{R_g T}{nF} \ \ln\left(1 - \frac{i}{i_L}\right)$	i_L	*L*, *M*, *H* 9, 1125, 1216	*L*, *M*, *H* 10, 505, 1001	mA cm^{-2}	From η_{MT} and η_{conc}

Table 4
Tafel kinetic parameters for the anode and cathode for different humidification conditions. The exchange current densities were corrected for the partial pressure of oxygen as described in Section 1.

		b (V decade^{-1})			i_0 (mA cm^{-2})		
		Anode	Cathode	Total	Anode	Cathode	Total
Baseline	Oxygen	0.008	0.068	0.069	5.54E−05	0.66E−09	0.66E−09
	Heliox	0.011	0.076	0.076	3.99E−05	1.73E−09	1.15E−09
	Air	0.006	0.073	0.073	7.70E−05	1.13E−09	0.92E−09
Flooding	Oxygen	0.019	0.067	0.073	2.05E−04	0.18E−09	0.51E−09
	Heliox	0.025	0.060	0.071	1.73E−04	0.04E−09	0.12E−09
	Air	0.005	0.069	0.069	5.66E−05	0.21E−09	0.17E−09
Drying	Oxygen	0.004	0.068	0.060	7.13E−11	0.23E−09	0.02E−09
	Heliox	0.004	0.147	0.085	6.68E−06	53.0E−09	0.03E−09
	Air	0.004	0.068	0.060	7.13E−11	0.23E−09	0.02E−09

Table 5
Diffusion coefficient of water in the respective gases, and thermal conductivity of air, helium and nitrogen.

	K (mW m^{-1} K^{-1})						D (m^2 s^{-1})
T (K)	100	200	300	400	500	600	298
Air	9.4	18.4	26.2	33.3	39.7	45.7	2.51×10^{-5}
Helium	75.5	119.3	156.7	190.6	222.3	252.4	3.14×10^{-4}
Nitrogen	9.8	18.7	26	32.3	38.3	44	3.90×10^{-5}

where p_{O_2} is the pressure, m is the reaction order and $b = 2.303\,RT/F$. Taking the logarithms on both sides, and partial derivatives with respect to p_{O_2}, three equations can relate p_{O_2} to linear functions of m under constant potential, constant current, and at zero overpotential, respectively. With this analysis, it is possible to use a pair of performance curves (with air and oxygen) to determine the ORR reaction order, MEA state at startup, and mass-transfer limitations in kinetically controlled currents. Following the full analysis from several sources [2,5,28], the voltage difference between the two curves can be derived (Eq. (11)).

$$\Delta E_{O_2/air} = E_{O_2} - E_{air} = m \times (R_g \times T)/F \times \ln\left(\frac{p_{O_2}}{p_{air}}\right) \quad (11)$$

For operation under normal conditions, the anodic contributions in our measurements represent 5–18.5% of the total cell potential losses, depending on the current density. These percentages were calculated as the ratios of anode and cathode overpotentials to the total cell potential (see Fig. 5)

Under normal conditions, the activation overpotential is the most significant anodic loss. However, the anodic diffusion and concentration losses (as defined in our nomenclature) also play a major role, contributing up to 30% of the total losses at the anode. Since the fuel composition was not altered, we can only speculate that these changes are due to an indirect effect (from the cathode side) when the cell is operated under varying oxygen concentrations (i.e., increasing anodic losses for operation with oxygen, heliox and air.)

Following the nomenclature in Section 3.1, the different overpotentials can be calculated from H_2/air polarization data for simulated flooding and drying conditions (Fig. 6) and compared to the corresponding overpotentials from the baseline performance. As illustrated, all the overpotentials changed with deviations from the baseline conditions at 100% RH.

During a simulated flooding event, the anodic overpotential increases with the current density. The increase can be related to water production increases at the cathode, and larger water fluxes toward the anode. The resulting liquid water within the porous MEA layers reduces the effective porosity on both electrodes. The reduced void volume and the lower concentration of reactants result in an overall lower fuel cell performance.

Under drying conditions, the anodic contributions increase rapidly as soon as the overall fuel cell potential starts to deviate from its value at 100% RH conditions. As the current and the required reactant flow rates increase, the ionomer in the catalyst layer becomes dehydrated increasing the resistances to proton transport.

The results show that the anodic overpotentials increase significantly, reinforcing the importance of including these losses in the analysis. During flooding conditions, the anodic overpotentials increase to 10–23% of the total potential loss contributions (increasing proportionally with current density), mainly due to water accumulation. During dry conditions, the anodic overpotentials contribute up to the 30% of the total performance losses, mainly due to the lack of proton mobility (e.g., the inability to

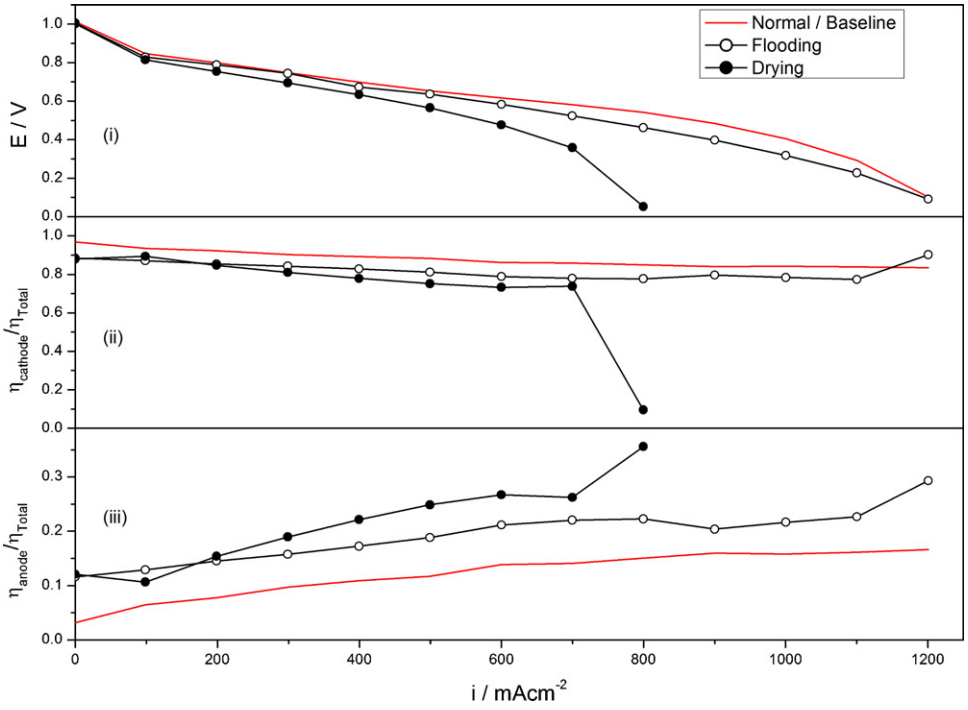

Fig. 5. (i) Polarization curves for all humidity conditions and air as cathodic gas feed. (ii) Cathode overpotential divided by the total overpotential. (iii) The anode overpotential divided by the total overpotential. The red lines show the cathode and anode behaviour during normal conditions. (For interpretation of the references to colour in this figure legend, the reader is referred to the web version of this article.)

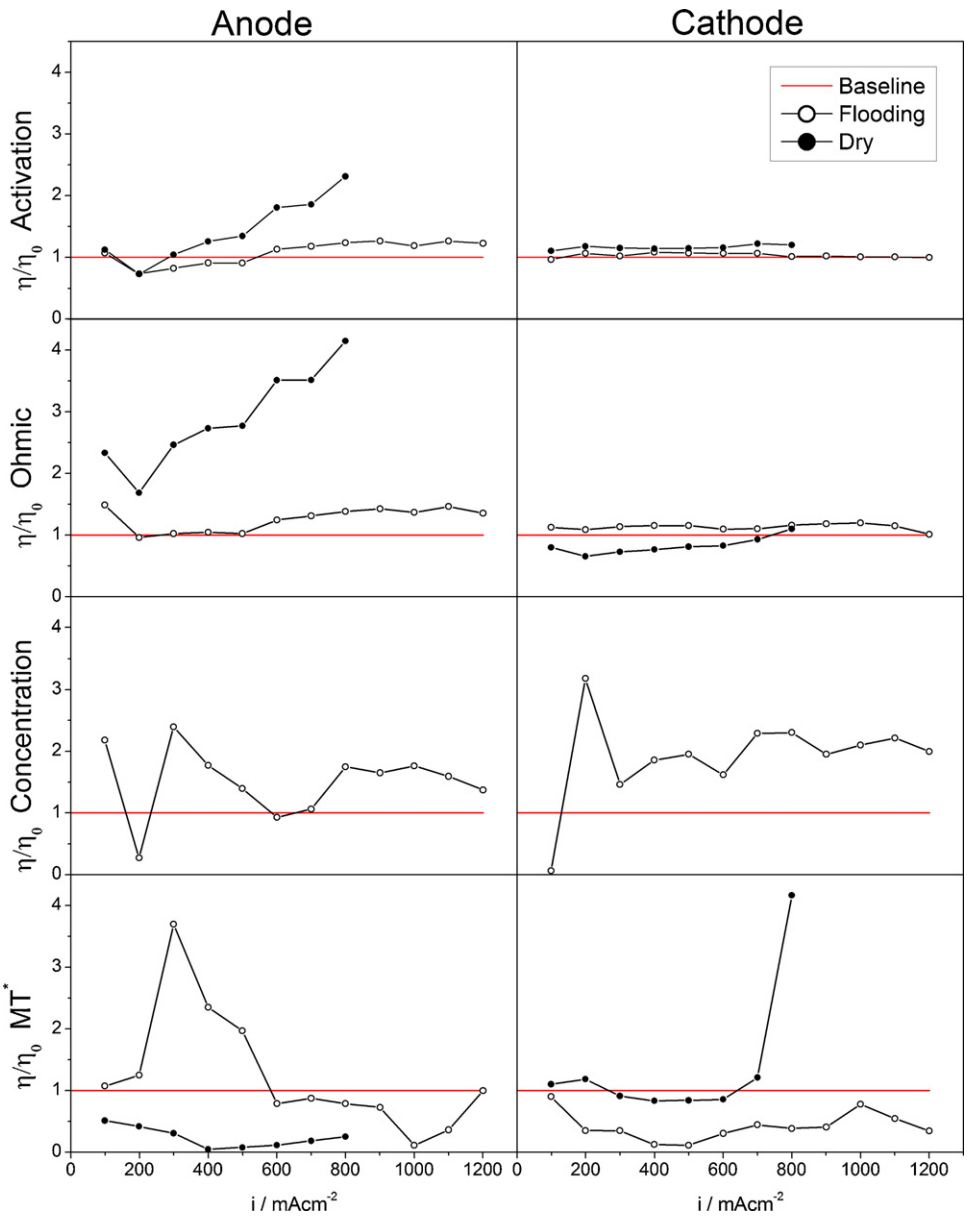

Fig. 6. Anodic and cathodic overpotentials of dry and flooding conditions normalized against normal conditions (baseline). η/η_0 MT (mass transport) includes concentration losses for dry conditions as heliox dries the cell faster and the potential response is lower than the potential response when using air.

solvate the proton completely), shown by the increases in anodic resistances.

With increasing current density, the calculated activation losses remain approximately constant for the cathode, but they increase in the anode, particularly under dry conditions. This suggests, that the hydrogen oxidation reaction is affected, as noted by Weng [29].

Table 4 shows the calculated experimental kinetic parameters based on the Tafel equation. The calculation of the exchange current density takes into account the partial pressure of the gas, the loading and the mass-specific surface area (this value was estimated to be $60\,m^2_{Pt}\,g^{-1}_{Pt}$ from the literature [2]). The values of both the exchange current density and the Tafel slope of the cathode are in good agreement with published data ($0.8–8.7 \times 10^{-9}\,A\,cm^{-2}$ and $0.053–0.066\,V\,decade^{-1}$, respectively) [2]. The total values shown in Table 4 refer to the sum of anode and cathode contributions, and it assumes that the anode overpotentials are negligible. However, this assumption is only valid for normal humidification conditions.

Considering the limitations of the Butler–Erdy–Grutz–Volmer equation and those of the Tafel approximation it is evident that the anode kinetics are fast compared to the cathode kinetics. However, the exchange current densities of the anode under dry conditions are as low as those at the cathode, when using oxygen or air as oxidant. These values indicate that the anodic contributions to the fuel cell losses should not be neglected, and that the Tafel approximation is not valid under drying conditions. The exchange current densities with heliox under dry conditions are not in agreement with the values of air and oxygen. This discrepancy may be due to the increased dehydration when using helium as the supporting gas. Water has a larger diffusivity in helium ($3.14 \times 10^{-4}\,m^2\,s^{-1}$) than in nitrogen ($3.90 \times 10^{-5}\,m^2\,s^{-1}$, about 10 times larger) and helium has a higher thermal conductivity as shown in Table 5. Hence, the gas temperature near the cathode electrode can be higher while running with heliox thereby increasing the amount of water vapour carrying more water and drying the MEA faster.

The concentration losses during flooding conditions increase by up to 3 times on the cathode and up to 2.5 times on the anode, compared to normal conditions. The gas partial pressure is reduced

by the total pressure change created by the presence of water. Moreover, the liquid water in the flow field channels during flooding creates greater pressure drops for both the anode and the cathode, as shown in Table 6. For the cathode, the pressure drop is highest when using air, then heliox and finally pure oxygen, due to the different mass flow rates. The different gases in the cathode also affect the anode because the water concentration increases, changing the diffusion flux from the cathode to the anode. This is reflected in the pressure drop of the anode that is highest when using oxygen, then heliox and finally air; implying that there is a higher concentration of liquid water in the flow-fields and probably in the MEA when running the fuel cell with pure oxygen. During flooding conditions, there is a higher pressure difference between the inlet (kept constant at 3.04 atm) and the outlet, as shown in Table 6. As both sides are flooded, we speculate that the water diffusion from the cathode to the anode is still the predominant mechanism of water transport through the membrane. The pressure drop is smaller during dry conditions at both the anode and the cathode, indicating the lack of liquid water and single-phase flow in agreement with the work of Basu et al. [30].

The mass transport overpotential decreased during flooding conditions for all current densities for the cathode, and for current densities above 300 mA cm^{-2}, for the anode. Possible causes

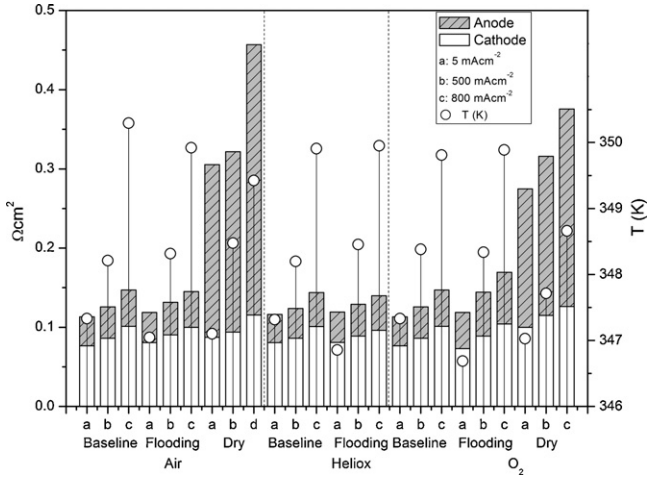

Fig. 7. Average ohmic resistances (stacked) and temperature averages (white open circles) for anode and cathode during normal, flooding, and dry conditions for the air and oxygen. Only normal and flooding conditions are presented for heliox.

a)

In	1	2	3	4
1	1.54 A 74.99 °C η_a = 0.089 V η_c = 0.474 V	1.60 A 74.70 °C η_a = 0.088 V η_c = 0.474 V	1.63 A 75.24 °C η_a = 0.089 V η_c = 0.474 V	1.64 A 74.88 °C η_a = 0.089 V η_c = 0.474 V
2	1.59 A 75.19 °C η_a = 0.088 V η_c = 0.474 V	1.72 A 75.23 °C η_a = 0.088 V η_c = 0.474 V	1.76 A 75.29 °C η_a = 0.088 V η_c = 0.474 V	1.77 A 75.30 °C η_a = 0.089 V η_c = 0.474 V
3	1.52 A 74.96 °C η_a = 0.088 V η_c = 0.475 V	1.66 A 75.11 °C η_a = 0.088 V η_c = 0.474 V	1.70 A 75.16 °C η_a = 0.088 V η_c = 0.474 V	1.69 A 75.26 °C η_a = 0.089 V η_c = 0.474 V
4	1.28 A 74.81 °C η_a = 0.087 V η_c = 0.475 V	1.39 A 75.02 °C η_a = 0.087 V η_c = 0.475 V	1.41 A 75.13 °C η_a = 0.087 V η_c = 0.475 V	1.47 A 74.71 °C η_a = 0.088 V η_c = 0.475 V

Out

b)

In	1	2	3	4
1	1.12 A 74.83 °C η_a = 0.110 V η_c = 0.481 V	1.19 A 74.10 °C η_a = 0.111 V η_c = 0.482 V	1.27 A 74.94 °C η_a = 0.110 V η_c = 0.482 V	1.26 A 74.53 °C η_a = 0.113 V η_c = 0.481 V
2	1.67 A 75.12 °C η_a = 0.120 V η_c = 0.477 V	1.80 A 75.06 °C η_a = 0.122 V η_c = 0.477 V	1.85 A 75.05 °C η_a = 0.123 V η_c = 0.477 V	1.84 A 74.83 °C η_a = 0.117 V η_c = 0.477 V
3	1.69 A 74.89 °C η_a = 0.124 V η_c = 0.470 V	1.82 A 74.87 °C η_a = 0.129 V η_c = 0.469 V	1.88 A 74.83 °C η_a = 0.129 V η_c = 0.468 V	1.85 A 74.99 °C η_a = 0.124 V η_c = 0.469 V
4	1.44 A 74.86 °C η_a = 0.118 V η_c = 0.470 V	1.53 A 74.94 °C η_a = 0.121 V η_c = 0.470 V	1.56 A 75.09 °C η_a = 0.121 V η_c = 0.470 V	1.55 A 74.41 °C η_a = 0.119 V η_c = 0.470 V

Out

c)

In	1	2	3	4
1	0.34 A 74.38 °C η_a = 0.149 V η_c = 0.484 V	0.23 A 73.62 °C η_a = 0.142 V η_c = 0.484 V	0.23 A 74.49 °C η_a = 0.144 V η_c = 0.484 V	0.33 A 74.10 °C η_a = 0.150 V η_c = 0.484 V
2	1.12 A 74.67 °C η_a = 0.133 V η_c = 0.479 V	1.15 A 74.59 °C η_a = 0.136 V η_c = 0.479 V	1.18 A 74.57 °C η_a = 0.139 V η_c = 0.479 V	1.27 A 74.74 °C η_a = 0.140 V η_c = 0.479 V
3	2.12 A 74.58 °C η_a = 0.120 V η_c = 0.472 V	2.28 A 74.56 °C η_a = 0.124 V η_c = 0.471 V	2.34 A 74.55 °C η_a = 0.122 V η_c = 0.470 V	2.31 A 74.71 °C η_a = 0.123 V η_c = 0.471 V
4	2.41 A 74.60 °C η_a = 0.112 V η_c = 0.471 V	2.65 A 74.65 °C η_a = 0.108 V η_c = 0.469 V	2.74 A 74.83 °C η_a = 0.109 V η_c = 0.469 V	2.64 A 74.16 °C η_a = 0.116 V η_c = 0.469 V

Out

Fig. 8. Current distribution of air/H_2 for different operating conditions (a) 100% RH, (b) 50% RH, and (c) 0% RH. The current was kept constant at an average current density of 522 mA cm^{-2}. The cell is operated in co-flow, segment 1–1 and segment 4–4 are the segments where the inlet and outlet are located, respectively.

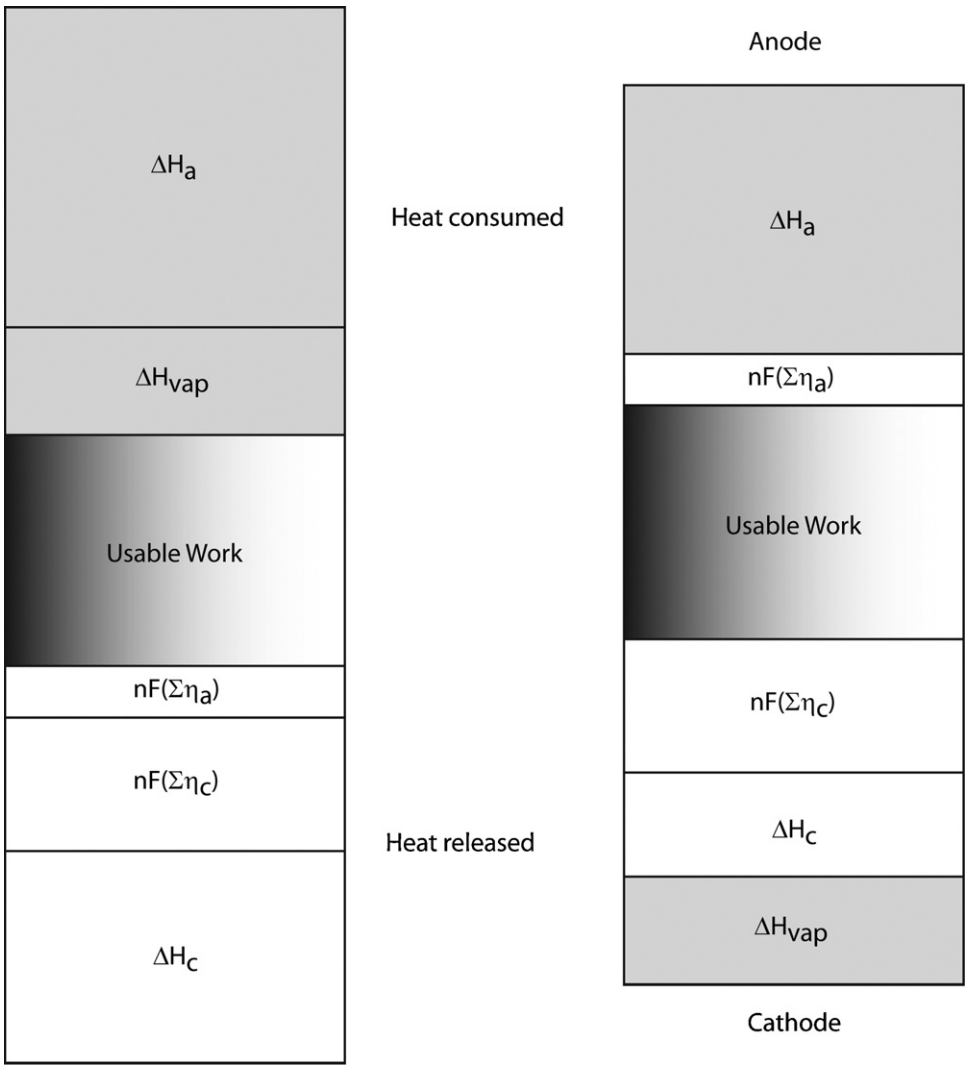

Fig. 9. Fuel cell energy profiles. The gray areas represent the heat consumed, the shaded area the usable work and the areas in white the released heat.

include the differences in diffusivity and thermal conductivity between helium and nitrogen, and convective transport by the differences in reactant flow rates. The analysis based on diffusivity differences is only valid when the gas is not completely saturated (i.e., if the gas is saturated, the water content in the gas only depends on the temperature).

Under dry conditions, the mass transport and concentration losses cannot be isolated because the heliox dries the MEA more rapidly than air as explained before [2,10]. Therefore, the limiting current is smaller when heliox is used. The mass transport and concentration overpotentials for the dry case increase approximately 400% on the cathode closer to the limiting current, mainly due to the lack of ionic movement through the dehydrated MEA. For the anode, the highest mass transport and concentration losses occur at low current densities, only reducing after larger amounts of water are produced.

Average ohmic resistances are shown for the 3 gas compositions in Fig. 7. The ohmic losses remain fairly constant for the cathode. However, the anodic losses increase, especially under dry conditions. The average temperature of the fuel cell segments, measured by the thermistors in the middle of the current collectors in the PCB, slightly increases with current density (3–5° from 5 to 800 mA cm^{-2}). The increase is lower under dry conditions, especially for oxygen, as shown in Fig. 7. As evaporation is endothermic, drying conditions provide additional cooling. The enthalpy of evaporation at 75 °C is 41.06 kJ mol^{-1}, so this is a significant effect, but the local cooling is masked by the constant temperature provided by the heating plates.

3.2. Overpotential distribution

To understand the effect of the in-plane gradients on the overpotentials, a segmented cell was used to monitor the current distribution. Fig. 8 illustrates the current, temperature and overpotentials measured under three inlet relative humidity conditions: (a) 100% RH, (b) 50% RH and (c) 0% RH (dew point <0 °C).

The cell is operated in co-flow and the hydrogen and oxygen concentrations decrease from the top to the bottom. Under 100% RH conditions the temperature remains fairly constant throughout the active area (±2 °C), indicating homogeneous cooling, and no significant temperature effects on the current measurements. The overall current for the fuel cell was held constant at 25 A (an average of 522 mA cm^{-2}). The segments start with a uniform current density between 1.3 and 1.8 A per segment or 0.425 and 0.588 A cm^{-2}.

When the humidity is lowered and the membrane starts to dehydrate, the segments closer to the inlet (row 1) start producing less current and the middle segments compensate for this current loss. The anode overpotential at row 1 is low compared to the other

Table 6
Pressure drop values at the inlet and outlet of the fuel cell for all gases and conditions at 800 mA cm^{-2}.

Condition	Gas	ΔP_c (atm)	ΔP_a (atm)
Normal	Air	0.231	0.145
	Heliox	0.141	0.141
	Oxygen	0.029	0.15
Flooding	Air	0.247	0.17
	Heliox	0.154	0.176
	Oxygen	0.045	0.179
Drying	Air	0.124	0.104
	Oxygen	0.021	0.152

rows at 50% RH because the anodic overall average resistance is just starting to increase (0.119 Ωcm^2). However, considering that the ohmic losses are a function of the current, the value still suggests an increment in the anodic overpotentials. Also, the cathode overpotentials start to increase creating current and overpotential gradients that increase as the MEA dries. When the membrane is completely dehydrated, the highest current density is produced by the segments of row 3 and the segments closer to the outlet (row 4), while the segments closest to the inlet barely produce any current. Due to the increasing inhomogeneous dehydration of the MEA at dry conditions, the current in-plane gradients are larger and they create large heat differences in the catalyst layer. However, the water-heated plates transfer enough heat to maintain an approximate homogeneous temperature distribution in the graphite plates. The high thermal conductivity of the graphite compared to that of the GDL and electrode, reduces the measureable thermal gradients to only a fraction of the gradients which are present in the electrode.

The fuel cell potential depends on the overpotentials from the anode and the cathode as shown in Fig. 9. Assuming that all the water produced is evaporated under dry conditions, the heat profiles in the MEA change in accordance with the current and water produced. Fig. 10 shows these profiles of heat flux over the active area for both the anode and the cathode under dry conditions (assuming complete evaporation.) The heat profiles were only calculated for the dry condition, because it is unphysical to assume complete water evaporation under normal and flooding conditions. The power profiles were calculated based on the enthalpy of reaction for the anodic half-cell endothermic reaction (440.487 kJ mol^{-1} at 343 K), the enthalpy of reaction for the cathodic half-cell exothermic reaction (−683.371 kJ mol^{-1} at 343 K), the enthalpy of vaporization of water (41.787 kJ mol^{-1} at 343 K) using Eqs. (10), (11), and (12), for the fuel cell. The total heat released by the fuel cell is defined by the heat of reactions for the fuel cell (cathode and anode) minus the electrical work.

$$Q_{\text{Total}} = Q_c + Q_a - \text{Work} \tag{12}$$

$$Q_c = \Delta H_{343,c} - \Delta G_{343,c} - n \times F \times \Sigma(\eta_c) + \Delta H_{\text{vap}} \tag{13}$$

$$Q_a = \Delta H_{343,a} - \Delta G3_{43,a} - n \times F \times \Sigma(\eta_a) \tag{14}$$

As expected, the maximum heat production occurs where the largest current densities are, but the largest usable work is in row 3 for the dry conditions. The difference between the anode and the cathode is lower in the initial row (closer to the inlets) because there is less current and consequently less ohmic heating. These localized heat differences can create stresses that may damage the MEA, as discussed by Gasteiger et.al. [2] and Pharoah and Burheim [22]

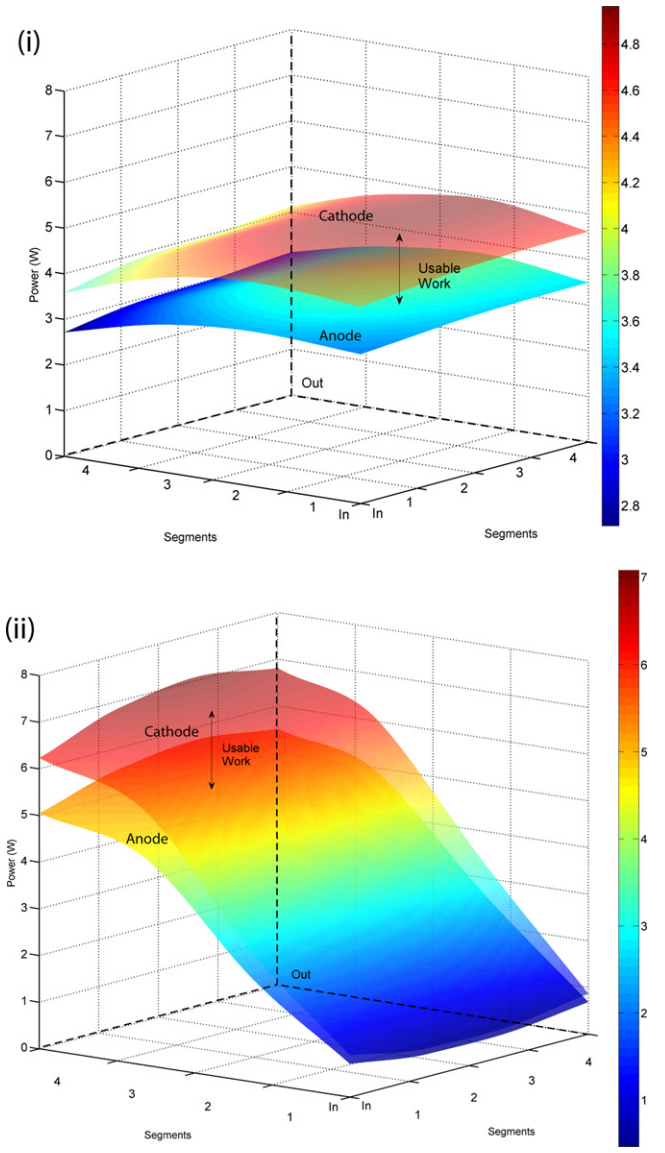

Fig. 10. In-plane heat generation distribution of the cathode (top) and anode (bottom) catalyst layers for 100% RH (i) and under dry conditions (ii). No heat of evaporation is considered for the 100% RH case. The values were calculated using the spatially resolved current generation and the overpotential values and then interpolated to create a continuous function.

4. Conclusions

The anodic and cathodic individual overpotentials were obtained in a segmented and unsegmented fuel cell via reference electrodes and multi-component gas analysis. The results show that the anodic overpotentials cannot be ignored, even if the anode conditions remain constant and changes are imposed on the cathode only. The anode can contribute up to 20% of the losses under normal and flooding conditions and above 30% under dry conditions. The measured and calculated kinetic parameters support these results: under dry conditions the exchange current density of the anode is smaller than that of the cathode.

The anode overpotentials are affected by the oxygen concentration that limits the cathodic reaction and has an indirect effect on the anode. The anode potential is also largely affected by the current distribution as the *iR* losses contribute to about 30% of its total overpotentials.

The activation losses for both the anode and the cathode are the largest, even for state-of-the-art electrodes [5]. Cathode

activation overpotentials are the largest, but anodic overpotentials can be significant, especially under dry conditions. The activation overpotentials increase in the order from normal to flooding to dry conditions. Under dry conditions, the membrane conductivity decreases leading to higher ionic resistances. Ohmic losses increase with current density and vary depending on the humidity conditions. These conditions also affect the temperature profile in the fuel cell by, for example, cooling it under dry conditions due to water vaporization. Based on the calculated overpotentials and enthalpies of the half-cell reactions, it was possible to calculate the temperature distribution over the active area. The results show that the heat from the cathodic exothermic reaction is highly affected by the water vaporization for dry conditions, and that large current gradients exist. However, in order to confirm these temperature profiles, it would be necessary to measure the temperature as close to the catalyst layers as possible.

The activation, ohmic, concentration and mass transport losses increase proportionally with current density and vary locally with different gradients across the fuel cell, especially during dry conditions. By combining reference electrodes with current mapping, it is possible to measure and calculate different parameters that can be used for modeling, and to understand the behavior of the anode and the cathode independently.

Acknowledgements

The authors would like to thank CONACYT and NSERC for the financial support of this project.

References

[1] M. Inaba, T. Kinumoto, M. Kiriake, R. Umebayashi, A. Tasaka, Z. Ogumi, Gas crossover and membrane degradation in polymer electrolyte fuel cells, Electrochimica Acta 51 (2006) 5746–5753.
[2] H.A. Gasteiger, W. Gu, R. Makharia, M.F. Mathias, B. Sompalli, in: W. Vielstich, A. Lamm, H.A. Gasteiger (Eds.), Hanbook of Fuel Cells: Fundamentals, Technologies, and Applications, John Wiley & Sons, New York, 2003 (3 Chapter 46).
[3] S.B. Adler, B.T. Henderson, M.A. Wilson, D.M. Taylor, R.E. Richards, Reference electrode placement and seals in electrochemical oxygen generators, Solid State Ionics 134 (2000) 35–42.
[4] S.J.C. Cleghorn, J. Kolde, W. Liu, Catalyst coated composite membranes, in: W. Vielstich, A. Lamm, H.A. Gasteiger (Eds.), Hanbook of Fuel Cells: Fundamentals, Technologies, and Applications, John Wiley & Sons, New York, 2003 (3 Chapter 44).
[5] D.L. Wood, I.I.I.R.L. Borup, Estimation of mass-transport overpotentials during long-term PEMFC operation, Journal of the Electrochemical Society 157 (2010) B1251–B1262.
[6] C.H. Hamann, A. Hamnett, W. Vielstich, Electrochemistry, Wiley-VCH, 1998.
[7] O. Herrera, W. Mérida, D.P. Wilkinson, Sensing electrodes for failure diagnostics in fuel cells, Journal of Power Sources 190 (2009) 103–109.
[8] D.B. Spry, M.D. Fayer, Proton transfer and proton concentrations in protonated nafion fuel cell membranes, The Journal of Physical Chemistry B 113 (2009) 10210–10221.
[9] H. Kuhn, A. Wokaun, G.G. Scherer, Exploring single electrode reactions in polymer electrolyte fuel cells, Electrochimica Acta 52 (2007) 2322–2327.
[10] R.S. Fu, X. Zhang, U. Pasaogullari, Heat and mass transfer in polymer electrolyte fuel cells in ultra-low humidity operation, ECS Transactions 25 (2009) 323–332.
[11] T. Kim, S. Lee, H. Park, A study of water transport as a function of the micro29 porous layer arrangement in PEMFCs, International Journal of Hydrogen Energy 35 (2010) 8631–8643.
[12] Z. Siroma, R. Kakitsubo, N. Fujiwara, T. Ioroi, S.-I. Yamazaki, K. Yasuda, Compact dynamic hydrogen electrode unit as a reference electrode for PEMFCs, Journal of Power Sources 156 (2006) 284–287.
[13] J. St-Pierre, D.P. Wilkinson, S. Knights, M.L. Bos, Relationships between water management, contamination and lifetime degradation in PEFC, Journal of New Materials for Electrochemical Systems 3 (2000) 99–106.
[14] Y.W. Rho, S. Srinivasan, Y.T. Kho, O.A. Velev, Mass transport phenomena in proton exchange membrane fuel cells using O[sub 2]/He, O[sub 2]/Ar, and O[sub 2]/N[sub 2] mixtures, Journal of the Electrochemical Society 141 (1994) 2089–2096.
[15] Y.W. Rho, O.A. Velev, S. Srinivasan, Y.T. Kho, Mass Transport phenomena in proton exchange membrane fuel cells using O[sub 2]/He, O[sub 2]/Ar, and O[sub 2]/N[sub 2] mixtures, Journal of the Electrochemical Society 141 (1994) 2084–2089.
[16] S.J.C. Cleghorn, C.R. Derouin, M.S. Wilson, S. Gottesfeld, A printed circuit board approach to measuring current distribution in a fuel cell, Journal of Applied Electrochemistry 28 (1998) 663–672.
[17] K. Inman, X. Wang, B. Sangeorzan, Design of an optical thermal sensor for proto1 n exchange membrane fuel cell temperature measurement using phosphor thermometry, Journal of Power Sources 195 (2010) 4753–4757.
[18] H. Kuhn, B. Andreaus, A. Wokaun, G.G. Scherer, Electrochemical impedance spectroscopy applied to polymer electrolyte fuel cells with a pseudo reference electrode arrangement, Electrochimica Acta 51 (2006) 1622–1628.
[19] D. Natarajan, T.V. Nguyen, Experimental investigation of spatial-temporal current distribution in a PEM fuel cell, in: AIChE 2000 Annual Meeting, Symposium on Fuel Cells, Systems and Processors II, November 12–17, Los Angeles, CA, 2000.
[20] A. Schröder, K. Wippermann, J. Mergel, W. Lehnert, D. Stolten, T. Sanders, T. Baumhöfer, D.U. Sauer, I. Manke, N. Kardjilov, A. Hilger, J. Schloesser, J. Banhart, C. Hartnig, Combined local current distribution measurements and high resolution neutron radiography of operating direct methanol fuel cells, Electrochemistry Communications 11 (2009) 1606–1609.
[21] J. Stumper, S.A. Campbell, D.P. Wilkinson, M.C. Johnson, M. Davis, In-situ methods for the determination of current distributions in PEM fuel cells, Electrochimica Acta 43 (1998) 3773–3783.
[22] J.G. Pharoah, O.S. Burheim, On the temperature distribution in polymer electrolyte fuel cells, Journal of Power Sources 195 (2010) 5235–5245.
[23] O.E. Herrera, W. Merida, D.P. Wilkinson, New reference electrode approach for fuel cell performance evaluation, ECS Transactions 16 (2008) 1915–1926.
[24] A. Hashibon, S. Raz, I. Riess, Preferred position for the reference electrode in solid state electrochemistry, Solid State Ionics 149 (2002) 167–176.
[25] D. Gerteisen, Realising a reference electrode in a polymer electrolyte fuel cell by laser ablation, Journal of Applied Electrochemistry 37 (2007) 1447–1454.
[26] J. Zhang, R.N. Carter, P.T. Yu, W. Gu, F.T. Wagner, H.A. Gasteiger, Fuel cells – proton-exchange membrane fuel cells|catalysts: life-limiting considerations, Encyclopedia of Electrochemical Power Sources (2009) 626–638.
[27] H. Lv, S. Mu, N. Cheng, M. Pan, Nano-silicon carbide supported catalysts for PEM fuel cells with high electrochemical stability and improved performance by addition of carbon, Applied Catalysis B: Environmental 100 (2010) 190–196.
[28] S.S. Kocha, Principles of MEA preparation, in: Hanbook of Fuel Cells: Fundamentals, Technologies, and Applications, 2003, pp. 538–565 (3 Chapter 43).
[29] F.-B. Weng, B.-S. Jou, C.-W. Li, A. Su, S.-H. Chan, The effect of low humidity on the uniformity and stability of segmented PEM fuel cells, Journal of Power Sources 181 (2008) 251–258.
[30] S. Basu, M.W. Renfro, B.M. Cetegen, Spatially resolved optical measurements of water partial pressure and temperature in a PEM fuel cell under dynamic operating conditions, Journal of Power Sources 162 (2006) 286–293.